

UC Santa Barbara

UC Santa Barbara Previously Published Works

Title

Probing material absorption and optical nonlinearity of integrated photonic materials

Permalink

<https://escholarship.org/uc/item/7q85k9nz>

Journal

Nature Communications, 13(1)

ISSN

2041-1723

Authors

Gao, Maodong
Yang, Qi-Fan
Ji, Qing-Xin
et al.

Publication Date













2022

DOI

10.1038/s41467-022-30966-5

Peer reviewed

Probing material absorption and optical nonlinearity of integrated photonic materials

Maodong Gao ^{1,5}, Qi-Fan Yang^{1,5}, Qing-Xin Ji ^{1,5}, Heming Wang ¹, Lue Wu ¹, Boqiang Shen ¹, Junqiu Liu ², Guanhao Huang², Lin Chang ³, Weiqiang Xie³, Su-Peng Yu ⁴, Scott B. Papp ⁴✉, John E. Bowers ³✉, Tobias J. Kippenberg ²✉ & Kerry J. Vahala ¹✉

Optical microresonators with high quality (Q) factors are essential to a wide range of integrated photonic devices. Steady efforts have been directed towards increasing microresonator Q factors across a variety of platforms. With success in reducing microfabrication process-related optical loss as a limitation of Q , the ultimate attainable Q , as determined solely by the constituent microresonator material absorption, has come into focus. Here, we report measurements of the material-limited Q factors in several photonic material platforms. High- Q microresonators are fabricated from thin films of SiO_2 , Si_3N_4 , $\text{Al}_{0.2}\text{Ga}_{0.8}\text{As}$, and Ta_2O_5 . By using cavity-enhanced photothermal spectroscopy, the material-limited Q is determined. The method simultaneously measures the Kerr nonlinearity in each material and reveals how material nonlinearity and ultimate Q vary in a complementary fashion across photonic materials. Besides guiding microresonator design and material development in four material platforms, the results help establish performance limits in future photonic integrated systems.

¹T. J. Watson Laboratory of Applied Physics, California Institute of Technology, Pasadena, CA 91125, USA. ²Institute of Physics, Swiss Federal Institute of Technology Lausanne (EPFL), Lausanne CH-1015, Switzerland. ³ECE Department, University of California Santa Barbara, Santa Barbara, CA 93106, USA. ⁴National Institute of Standards and Technology, Boulder, CO 80305, USA. ⁵These authors contributed equally: Maodong Gao, Qi-Fan Yang, Qing-Xin Ji. ✉email: scott.papp@nist.gov; jbowers@ucsb.edu; tobias.kippenberg@epfl.ch; vahala@caltech.edu

Performance characteristics of microresonator-based devices improve dramatically with increasing Q factor¹. Nonlinear optical oscillators, for example, have turn-on threshold powers that scale inverse quadratically with Q factor^{2–4}. The fundamental linewidth of these and conventional lasers also vary in this way^{5–7}. In other areas including cavity quantum electrodynamics⁸, integrated quantum optics^{9–12}, cavity optomechanics¹³, and sensing¹⁴, a higher Q factor provides at least a linear performance boost. In recent years, applications that rely upon these microresonator-based phenomena, including microwave generation¹⁵, frequency microcomb systems¹⁶, high-coherence lasers^{7,17,18} and chip-based optical gyroscopes^{19–21}, have accelerated the development of high- Q photonic-chip systems^{18,22–31}.

Q factor is determined by material losses, cavity loading (i.e., external waveguide coupling), and scattering losses (see Fig. 1a). To increase Q factor, there have been considerable efforts focused on new microfabrication methods and design techniques that reduce scattering loss associated with interface roughness^{22,32,33} and coupling non-ideality^{34,35}. Impressive progress has resulted in demonstrations of high- Q microresonator systems with integrated functionality^{36,37}, as well as resonators that are microfabricated entirely within a CMOS foundry¹⁸. With these advancements, attention has turned towards Q limits imposed by the constituent photonic material themselves. For example, the presence of water, hydrogen, trace metal ions^{33,38–41}, and other pathways^{42,43} are known to increase absorption. In this work, cavity-enhanced photothermal spectroscopy^{39,41,44–47} is used to determine the absorption-limited Q factor (Q_{abs}) and optical nonlinearity of state-of-the-art high- Q optical microresonators fabricated from four different photonic materials on silicon wafers.

Results and discussion

Images of the microresonators characterized in this study are shown in Fig. 1b, where the microresonators are SiO₂^{4,48} microdisks and Si₃N₄⁴⁷, Al_{0.2}Ga_{0.8}As^{26,27}, and Ta₂O₅⁴⁹ microrings. Details of the device fabrication processes are given in the “Methods”. Typical microresonator transmission spectra showing optical resonances are presented in Fig. 1b. The transmission spectra feature Lorentzian lineshapes, but in some cases are distorted by etalon effects resulting from reflection at the facets of the coupling waveguide. With such etalon effects accounted for (see “Methods”), the intrinsic (Q_0) and external (coupling) (Q_e) Q factors can be determined. The measured intrinsic Q_0 factors are 418 million, 30.5 million, 2.01 million, and 2.69 million, for SiO₂, Si₃N₄, Al_{0.2}Ga_{0.8}As, and Ta₂O₅ devices, respectively.

The microresonator intrinsic Q_0 is determined by scattering and absorption losses. In order to isolate the absorption loss contribution, cavity-enhanced photothermal spectroscopy is used. The principle is based on shift of the resonant frequencies of dielectric microresonators by the Kerr effect and the photothermal effect, both of which result from the refractive index dependence on the intracavity optical intensity. Because these two effects occur on very distinct time-scales (Kerr effect being ultrafast and photothermal effect occurring at a relatively slow thermal time scale from milliseconds to microseconds), it is possible to distinguish their respective contributions to resonant frequency shift and infer their nonlinear coefficients⁴⁵. Two distinct measurements are performed to determine the absorption-limited Q_{abs} . Here, they are referred to as the “sum measurement” and “ratio measurement”. In the sum measurement, resonant frequency shift is measured to obtain the sum of Kerr and photothermal effects. In the ratio measurement, the photothermal frequency response is measured to distinguish its contribution from the Kerr effect.

In the sum measurement, the microresonator is probed by a tunable laser whose frequency is slowly swept across a resonance from the higher frequency side of a resonance (i.e., blue-detuned side). The input light polarization is aligned to the fundamental TE (Si₃N₄, Al_{0.2}Ga_{0.8}As, and Ta₂O₅) or TM (SiO₂) mode of the microresonator. In the case of SiO₂, because of the presence of multiple transverse modes, a fundamental mode well separated from other resonances was used so as to reduce the influence of mode interactions. The experimental setup is depicted in Fig. 2a. The frequency scan is measured by a radio-frequency calibrated Mach–Zehnder interferometer (MZI)⁵⁰. The probe laser frequency scan is sufficiently slow (i.e., quasi-static scan, see Supplementary Note III for details) to ensure that scan speed does not impact the observed lineshape through transient thermal processes within the microresonator. The transmission spectra exhibit a triangular shape⁵¹ as shown in Fig. 2b. Theoretical fittings of the transmission spectra are shown in red and discussed in “Methods”. Also, the cold resonance spectra (i.e., with very low waveguide power) measured under the same coupling conditions are plotted for comparison (dashed curve).

By changing the input pump laser power with a voltage-controlled optical attenuator (VOA), the quasi-static resonance shift $\delta\omega_0$ of the resonant frequency ω_0 versus the intracavity circulating optical energy density ρ (units of J·m^{−3}) is determined (see Supplementary Note III) and summarized in Fig. 2c. The observed linear dependence contains contributions from the Kerr self-phase modulation and photothermal effects as,

$$\frac{\delta\omega_0}{\omega_0} = -\frac{1}{\omega_0}(\alpha + g)\rho, \quad (1)$$

where α and g denote the photothermal coefficient and the Kerr coefficient given by:

$$\alpha = \bar{\kappa}_a \frac{\overline{\delta T}}{P_{\text{abs}}} \left(-\frac{\delta\omega_0}{\delta T} \right) V_{\text{eff}}, \quad (2)$$

$$g = \frac{\bar{n}_2}{\bar{n}_o \bar{n}_g} \omega_0 c.$$

Here, κ_a is the energy loss rate due to optical absorption, n_2 is the material Kerr nonlinear refractive index, n_o is the material refractive index, n_g is the material chromatic group refractive index, c is the speed of light in vacuum, P_{abs} is the absorbed optical power by the microresonator and δT is the change in temperature of the microresonator. The bar (e.g., \bar{n}_2) denotes the average value of the underneath variable weighted by the field distribution of the optical mode. The exact definition of each average is provided in Supplementary Note I.

The energy loss rate κ_a is related to the material absorption-limited Q_{abs} factor by

$$Q_{\text{abs}} = \frac{\omega_0}{\kappa_a}. \quad (3)$$

To determine $\bar{\kappa}_a$ and hence Q_{abs} from α , it is necessary to determine $V_{\text{eff}} \overline{\delta T}/P_{\text{abs}}$ and $\delta\omega_0/\delta T$. The effective mode volume V_{eff} is calculated using the optical mode obtained in finite-element modeling, and $\overline{\delta T}/P_{\text{abs}}$ is further calculated using the finite-element modeling with a heat source spatially distributed as the optical mode. The resonance tuning coefficient $\delta\omega_0/\delta T$ is directly measured by varying the temperature of the microresonator chip using a thermoelectric cooler (TEC), and the results are shown in Fig. 2d. Since the TEC heats the entire chip, the thermo-elastic effect of the silicon substrate contributes to the frequency shift and combines with the photothermal effect. However, this thermo-elastic contribution does not appear in the sum measurement, where the heating originates only from the

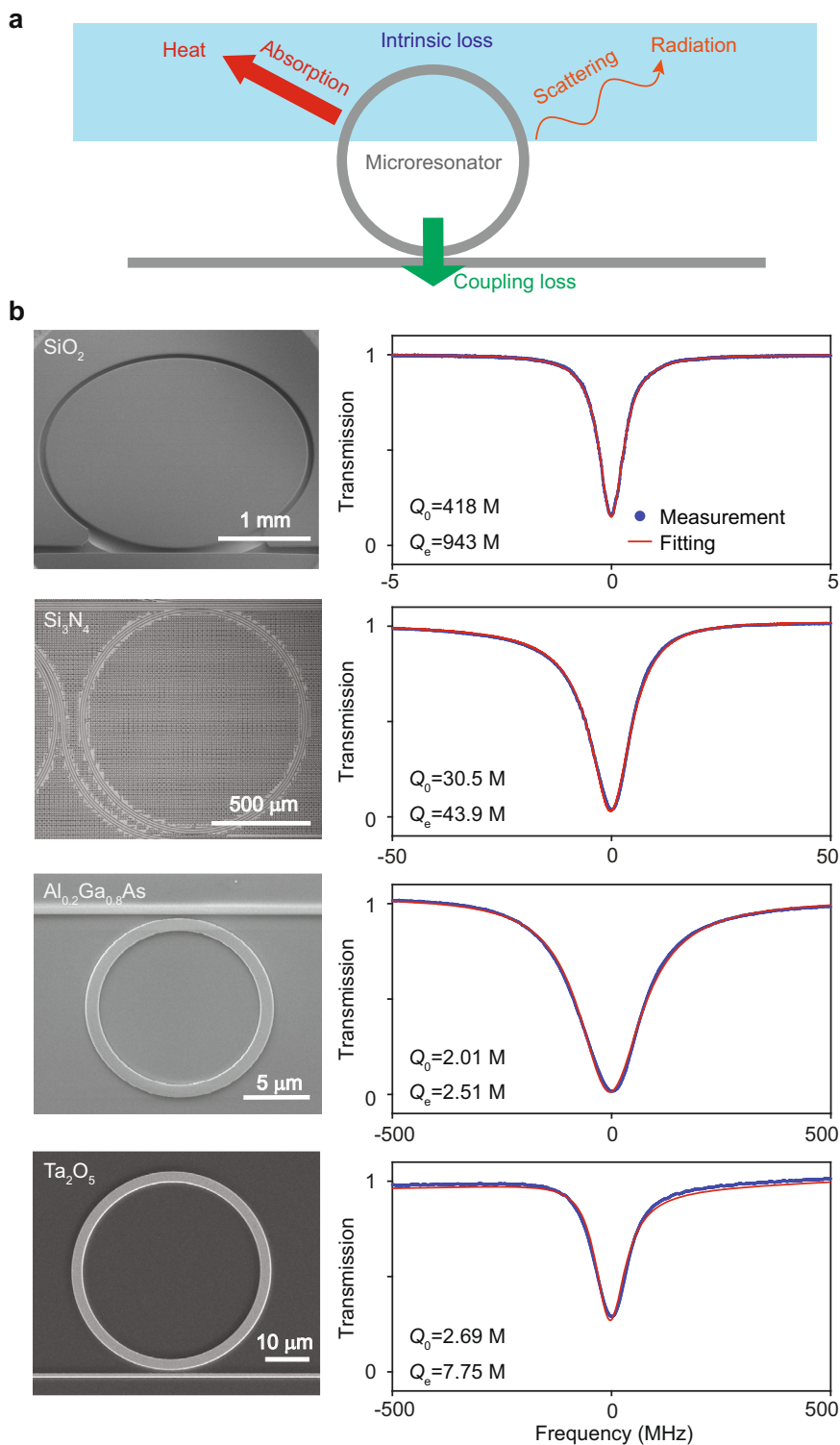


Fig. 1 High-Q optical microresonators characterized in this work. **a** Schematic showing optical loss channels for high-Q integrated optical microresonators. The loss channels include surface (and bulk) scattering loss and material absorption loss. The intrinsic loss rate is characterized by the intrinsic Q factor (Q_0). Bus waveguide coupling also introduces loss that is characterized by the external (coupling) Q factor (Q_e). **b** Left column: images of typical microresonators used in this study. Right column: corresponding low input-power spectral scans (blue points) with fitting (red). The intrinsic and external Q factors are indicated. M million.

optical mode. Thus, the thermal-elastic contribution of the silicon substrate must be deducted from the TEC measured results (see Supplementary Note I). Other effects that may lead to frequency shift or linewidth broadening, such as harmonic generation or multi-photon absorption, are not significant in the samples, as

confirmed by observing the coupling efficiency with respect to power (see Supplementary Note III).

The measurement associated with Eq. (1) wherein the sum contributions of Kerr and photothermal effects are measured is supplemented by a measurement that provides the ratio of these

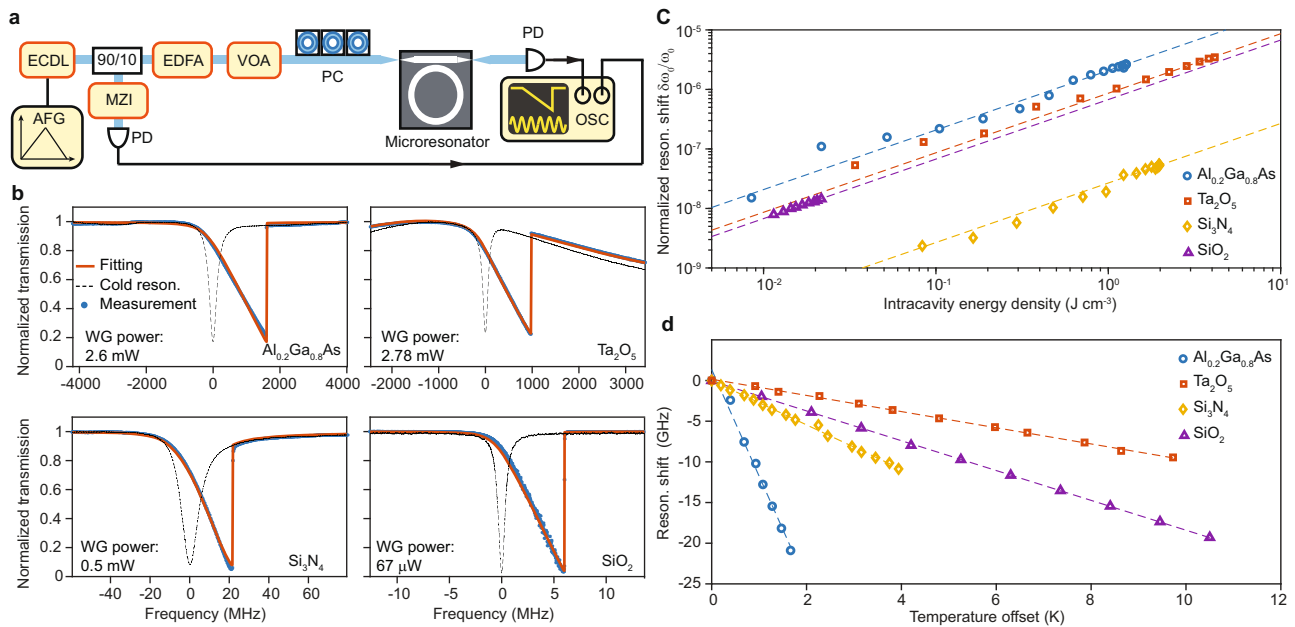


Fig. 2 The sum measurement. This experiment measures the sum of Kerr and photothermal nonlinear coefficients ($g + \alpha$). **a** Experimental setup. ECDL external-cavity diode laser, EDFA erbium-doped fiber amplifier, VOA voltage-controlled optical attenuator, PC polarization controller, PD photodetector, MZI Mach-Zehnder interferometer, AFG arbitrary function generator, OSC oscilloscope. For the SiO_2 measurement, the ECDL is replaced by a narrowlinewidth fiber laser to achieve a slower frequency tuning speed. As an aside, due to the narrower wavelength tuning range of the fiber laser, this measurement is only performed at 1550nm for SiO_2 . **b** Typical transmission spectra of microresonators showing the combined effect of photothermal and Kerr self-phase modulation. The input power in the bus waveguide is indicated. Theoretical fittings are plotted in red and discussed in “Methods”. The transmission spectra measured at low pump power are also plotted with dashed lines for comparison. WG power: optical power in the bus waveguide. **c** Measured resonant frequency shift versus intracavity power for microresonators based on different materials. Dashed lines are linear fittings of the measured data. The four traces have the same slope, which is a result of the proportional relation shown in Eq. (1). **d** Measured resonant frequency shift versus microresonator chip temperature for the four materials, with linear fittings. The fitted shift for $\text{Al}_{0.2}\text{Ga}_{0.8}\text{As}$, Si_3N_4 , SiO_2 , and Ta_2O_5 are -13.1 , -2.84 , -1.83 , and -0.996 , in units of $\text{GHz}\cdot\text{K}^{-1}$, respectively.

quantities. This second measurement takes advantage of the very different relaxation time scales of Kerr and photothermal effects. The experimental concept and setup are depicted in Fig. 3a, b. Pump and probe lasers are launched from opposite directions into the microresonator. The pump laser is stabilized to one resonance by monitoring the transmission signal and locking close to the center of the resonance. Pump power is modulated over a range of frequencies using a commercial lithium niobate electro-optic modulator driven by a vector network analyzer (VNA). Similarly, the probe laser is locked to another nearby resonance, and is slightly detuned from the center resonant frequency. Both probe and pump modes are fundamental spatial modes, but not necessarily in the same polarization state. For $\text{Al}_{0.2}\text{Ga}_{0.8}\text{As}$ and Ta_2O_5 , both pump and probe modes belong to the fundamental TE mode, while for Si_3N_4 , pump and probe modes belong to the fundamental TE and TM modes, respectively (see Supplementary Note III). It is also noted that this measurement was challenging to perform in the suspended SiO_2 microdisks on account of a very slow thermal diffusion process (see Supplementary Note IIIA). Instead, a published value of n_2 for SiO_2 ($2.2 \times 10^{-20} \text{ m}^2\cdot\text{W}^{-1}$) was used⁵².

With this arrangement, pump power modulation in the first resonance induces modulation of the output probe power in the second resonance, through the combined effect of Kerr- and photothermal-induced refractive index modulations. As illustrated in the inset of Fig. 3a, photothermal modulation determines the low frequency response in this measurement, while the Kerr effect determines the intermediate frequency response, and the highest corner frequency is set by the cavity dissipation rate

(see Methods). The probe frequency response measured for three different microresonators is presented in Fig. 3c. The response at very low frequencies is normalized to 0 dB. Both pump and probe laser powers are sufficiently low to minimize the thermal locking effect⁵¹. The plateau in the frequency response at low frequency gives the combined quasi-static contributions of photothermal and Kerr effects in the sum measurement (inset of Fig. 3a), while the high frequency response constitutes only the Kerr contribution. In addition, the Kerr effect here is the cross-phase modulation contribution (from the pump to the probe), while, as noted above, the Kerr self-phase modulation contribution appears in Eq. (1). These two effects are related by a cross-phase modulation factor γ determined by the mode combinations used (see Methods).

By numerically fitting the response curves (see Supplementary Note IIB and III), the ratio between Kerr and photothermal effects is extracted over a range of wavelengths and plotted in Fig. 3d.

Combining results from the above sum and ratio measurements, the photothermal and Kerr coefficients are obtained individually. The inferred absorption-limited Q_{abs} values measured over the telecommunication C-band for each material are summarized in Fig. 4a. It is worth mentioning that the SiO_2 microdisk measurement requires a narrow-linewidth, highly-stable fiber laser on account of the microresonator’s ultra-high Q factor. The use of the fiber laser limits the measurement range to near 1550 nm. A combined plot of the measured n_2 values (normalized by n_0^2) versus the absorption Q_{abs} is given in Fig. 4b (the n_2 of SiO_2 is taken from the literature⁵²). Also, for the case of critical coupling ($Q_e = Q_0$) and absorption-limited intrinsic Q factors ($Q_0 = Q_{\text{abs}}$), the parametric oscillation threshold per unit mode volume^{3,55,56} for a single material is shown

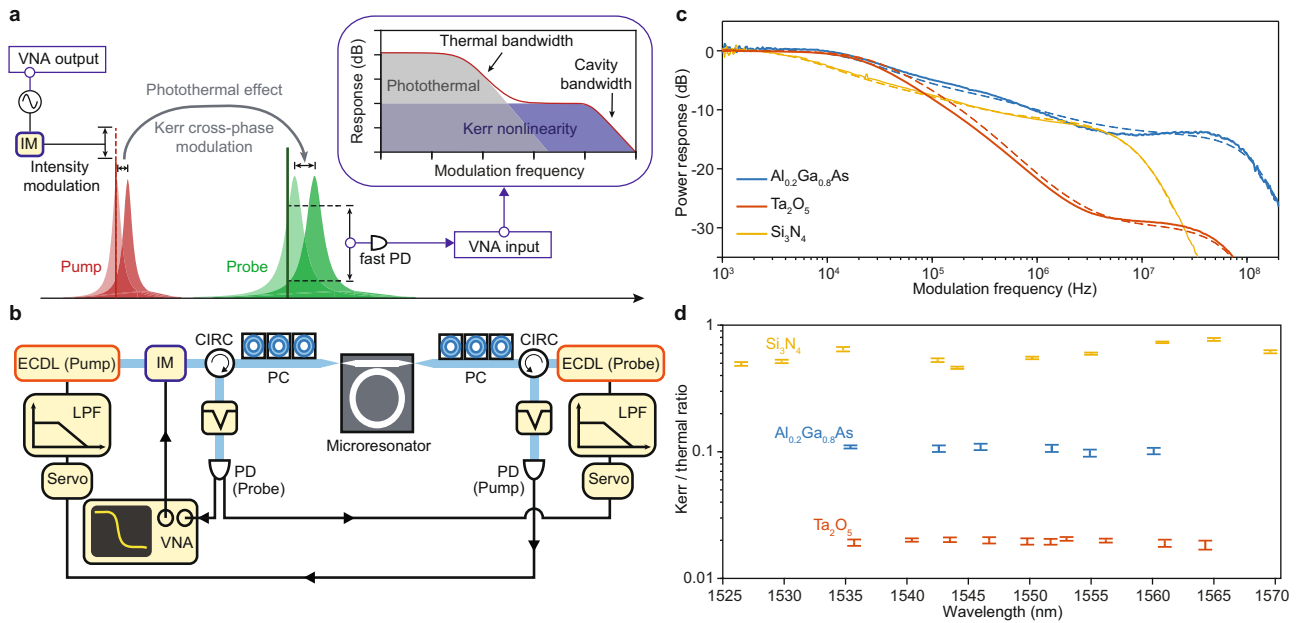


Fig. 3 The ratio measurement. This experiment measures the ratio of Kerr and photothermal nonlinear coefficients g/α . **a** Illustration of the ratio measurement. A pump laser is stabilized to a resonance and modulated by an intensity modulator. The intracavity power is thus modulated. As a result of the photothermal effect and Kerr cross-phase modulation, the frequency of a nearby resonance is also modulated. Another probe laser is stabilized near this resonance, and its transmission is monitored by a vector network analyzer (VNA). Inset: the modulation response distinguishes the photothermal and Kerr effects. **b** Experimental setup. IM intensity modulator, CIRC optical circulator, LPF low-pass filter, VNA vector network analyzer. **c** Typical measured response functions of the probe laser transmission as a function of modulation frequency Ω . Numerical fittings are shown as dashed curves. For modulation frequencies below 1 kHz, the probe response is suppressed by the servo feedback locking loop. Some artifacts appear around 1 kHz as a result of the servo control. Here the experimental trace is smoothed over 5 points. **d** Measured wavelength dependence of the ratios between the Kerr nonlinearity and photothermal effect for three materials. Vertical error bars give 95% confidence intervals.

by the dashed red iso-contours:

$$\frac{P_{th}}{V_{eff}} = \frac{n_o^2 \omega_o}{n_2 Q_{abs}^2 c}, \tag{4}$$

where V_{eff} is the effective mode volume. It should be noted that actual thresholds may be different if the optical field is not tightly confined in the core of the microresonator heterostructure.

The results described above are further summarized in Table 1, where, for SiO_2 and Si_3N_4 , the measured material absorption losses are lower than the present microresonator intrinsic losses. Therefore, improvement in microfabrication of SiO_2 and Si_3N_4 to reduce surface roughness, hence to reduce scattering losses, will benefit photonic integrated circuits using these materials. For $\text{Al}_{0.2}\text{Ga}_{0.8}\text{As}$ and Ta_2O_5 , the material losses are close to their respective intrinsic losses, which suggests that both material and scattering loss contributions should be addressed.

Overall, the absorption Q_{abs} values reported here should be viewed as state-of-the-art values that are not believed to be at fundamental limits. For example, silica glass in optical fiber exhibits loss (typically $0.2 \text{ dB}\cdot\text{km}^{-1}$)⁵⁷ that is over one order of magnitude lower than that reported in Fig. 4b. Likewise, Ta_2O_5 is the premier material for optical coatings employed, for example, in the highest performance optical clocks and gravitational-wave interferometers. However, Ta_2O_5 exhibits fascinating stoichiometry and crystallization effects, which require careful mitigation in deposition and processing. The material-limited Q of Ta_2O_5 and $\text{TiO}_2:\text{Ta}_2\text{O}_5$ has been measured to be 5 million and 25 million, respectively⁵⁸. Hence, the nanofabricated devices and precision-measurement technique reported here highlight the promise to optimize material-limited performance in the Ta_2O_5 platform. It is also noted that in $\text{Al}_{0.2}\text{Ga}_{0.8}\text{As}$, a compound semiconductor material, surface defects may generate mid-gap states⁴² which cause extra

material absorption loss. This loss mechanism will depend upon process conditions and intrinsic Q factors as high as 3.52 M for $\text{Al}_{0.2}\text{Ga}_{0.8}\text{As}$ have been reported elsewhere²⁷. Finally, some of the material parameters used in modeling are impacted by factors such as the film deposition method. For example, thermal conductivity of Ta_2O_5 can depend upon the deposition method as is reflected by a wide range of values available in the literature (see Supplementary Note IIID). Such effects could also impact other materials used in this study, but we have nonetheless relied upon bulk values and simplifications in modeling (see Supplementary Note IIC). Certain details in the simulation, e.g., heat dissipation rate into the air (see Supplementary Note IIC), are also possible contributing factors. Domain size in the finite element simulation have been optimized and not considered as an error source.

The current method also provides in situ measurement of n_2 for integrated photonic microresonators. We compare the n_2 values measured here with other reported values in Table 1. To consider how the nonlinearity varies between the four materials, third-order nonlinear susceptibility $\chi_{(3)}$ is calculated from the measured n_2 and compared with the linear susceptibility $\chi_{(1)}$. The Miller's rule^{59,60} $\chi_{(3)} \propto \chi_{(1)}^4$ relating the scaling of these two quantities is observed (see Supplementary Note IV).

In summary, the absorption loss and Kerr nonlinear coefficients of four leading integrated photonic materials have been measured using cavity-enhanced photothermal spectroscopy. The material absorption sets a practical limit on using these materials in microcavity applications. The Kerr nonlinear coefficients have also been characterized, and the results are consistent with a general trend relating to nonlinearity and optical loss. Overall, the results suggest specific directions where there can be an improvement in these systems as well as providing a way to predict future device performance.

Methods

Fabrication of optical microresonators. The SiO₂ microresonator is fabricated by thermally growing 8 μm thick thermal wet oxide on a 4 inch float-zone silicon wafer, followed by i-line stepper photolithography, buffered oxide etch, XeF₂ silicon isotropic dry etch, and thermal annealing^{4,48}. The Si₃N₄ microresonator is fabricated with the photonic Damascene process, including using deep-ultraviolet stepper lithography, etching, low-pressure chemical vapor deposition, planarization, cladding, and annealing⁴⁷. The Al_{0.2}Ga_{0.8}As microresonator is fabricated with an epitaxial Al_{0.2}Ga_{0.8}As layer bonded onto a silicon wafer with a 3 μm thermal SiO₂ layer, followed by GaAs substrate removal, deep ultraviolet patterning, inductively coupled plasma etching, and passivation with Al₂O₃ and SiO₂ cladding^{26,27}. The Ta₂O₅ microresonator is fabricated by ion-beam sputtering Ta₂O₅ deposition followed by annealing, electron-beam lithography, Ta₂O₅ etching, ultraviolet lithography, and dicing⁴⁹.

Experimental details. In the sum measurement, the scanning speed of the laser frequency is decreased until the mode's broadening as induced by the thermo-optic

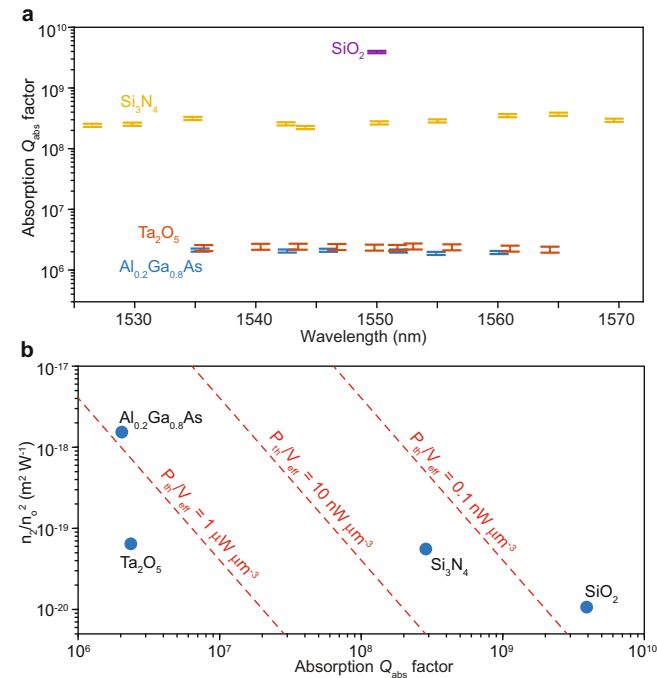


Fig. 4 Absorption Q_{abs} , nonlinear coefficients, and parametric oscillation threshold. **a** Measured absorption Q_{abs} factors at different wavelengths in the telecommunication C-band for the four materials. Vertical error bars give standard deviations of measurements. **b** Comparison of absorption Q_{abs} factors and normalized nonlinear index (n_2/n_0^2) for the four materials. Measured n_2 values are listed in Table 1. The n_2 of SiO₂ was not measured here and a reported value of $2.2 \times 10^{-20} \text{ m}^2 \text{ W}^{-1}$ is used. Parametric oscillation threshold for a single material normalized by the mode volume ($P_{\text{th}}/V_{\text{eff}}$) is indicated by the red dashed lines, assuming $\lambda = 1550 \text{ nm}$, intrinsic Q_0 equals material absorption Q , and $Q_e = Q_0$ (i.e., critical coupling condition).

Table 1 Properties of materials in current integrated high-Q microresonators at 1550 nm. Summary of material loss and nonlinearity.

Material	Growth method	Structure	n_0	Reported n_2 ($10^{-20} \text{ m}^2 \text{ W}^{-1}$)	n_2 ($10^{-20} \text{ m}^2 \text{ W}^{-1}$)	Q_{abs} (M)	σ_{abs} ($\text{dB} \cdot \text{m}^{-1}$)
SiO ₂	Wet oxidation	Amorphous	1.44	2.2	-	3900 ± 200	0.0065 ± 0.0003
Si ₃ N ₄	LPCVD	Amorphous	2.00	24	22 ± 1	290 ± 50	0.12 ± 0.02
Al _{0.2} Ga _{0.8} As	MBE	Crystal	3.28	2600	1700 ± 100	2.0 ± 0.2	28 ± 2
Ta ₂ O ₅	IBS	Amorphous	2.06	62	27 ± 3	2.4 ± 0.3	15 ± 2

LPCVD low-pressure chemical vapor deposition, MBE molecular beam epitaxy, IBS ion-beam sputtering. Propagation loss σ_{abs} induced by absorption is calculated as $\sigma_{\text{abs}} = (10/\ln 10)\omega_0\eta_g/(Q_{\text{abs}}c)$. Error indicates standard deviation. These numbers should be viewed as state-of-the-art values rather than fundamental limits. Possible systematic errors of measurement values are discussed in Supplementary Note IIC. The Q_{abs} for Ta₂O₅ is further discussed in Supplementary Note IIID. Reported n_2 values are taken from ref. 52 (SiO₂), ref. 53 (Si₃N₄), ref. 54 (Al_{0.2}Ga_{0.8}As) and ref. 49 (Ta₂O₅).

shift becomes stable (i.e., not influenced by the scan rate). Also, the waveguide input power is minimized such that it is well below the threshold of parametric oscillation. The power is calibrated using the photodetector voltage.

In the ratio measurement, the optical frequencies of the pump and probe lasers are locked to their respective cavity modes using a servo feedback with 1 kHz bandwidth. The pump laser is locked near the mode resonant frequency, while the probe laser is locked to the side of the resonance to increase transduction of refractive index modulation into transmitted probe power. The intensity modulator is calibrated in a separate measurement under the same driving power.

Fitting of spectra in the sum measurement. For Si₃N₄ and Ta₂O₅ devices, the transmission spectrum is the interference of a Lorentzian-lined mode resonance with a background field contributed by facet reflections of the waveguide. The transmission function of a cavity resonance is given by

$$T_{\text{res}} = 1 - \frac{\kappa_e}{\kappa/2 + i[\Delta - (\alpha + g)\rho]}, \quad (5)$$

where Δ is the cold-cavity laser-cavity detuning, α and g are the absorption and Kerr nonlinear coefficients, respectively, and ρ is the intracavity energy density as defined in the main text. The reflection at the two waveguide facets forms a low-finesse Fabry-Pérot resonator. Combining this waveguide reflection with the cavity resonance, the overall amplitude transmission is given by (see Supplementary Note II)

$$T \propto \left| \frac{T_{\text{res}}}{1 - rT_{\text{res}} \exp[i(-\Delta/\omega_{\text{FP}} + \phi)]} \right|^2, \quad (6)$$

where r is the reflectivity at the waveguide facet, ω_{FP} is the free spectral range of the facet-induced Fabry-Pérot cavity (in rad/s units), and ϕ is a constant phase offset.

In the experiment, the above quantities are fitted in three steps. First, ω_{FP} and r are obtained by measuring the transmission away from mode resonances. Next, loss rates κ and κ_e can be determined by measuring the transmission of the mode at a low probe power. Finally, launching higher power into the microresonator allows the mode broadening to be observed and the transmission is fitted with Eq. (6), where $(\alpha + g)$ is the fitting variable and other parameters are obtained from the previous steps. For Al_{0.2}Ga_{0.8}As and SiO₂ devices that have no Fabry-Pérot background, r can be set to zero and the first step in the above fitting procedure can be omitted. The fitting results are presented in Fig. 2b.

Fitting of response in the ratio measurement. The response of the probe mode resonant frequency $\tilde{\delta}_b$ as a result of pump power modulation \tilde{P}_{in} can be described by (see Supplementary Note II),

$$\frac{\tilde{\delta}_b(\Omega)}{\tilde{P}_{\text{in}}(\Omega)} = -\frac{\alpha\tilde{r}(\Omega) + \gamma g}{V_{\text{eff}}} \frac{2\eta_p}{i\Omega + \kappa_p/2}. \quad (7)$$

Where Ω is the pump power modulation frequency (in rad/s units), \tilde{P}_{in} is the modulation amplitude of the pump power, κ_p is the total loss rate of the pump mode, $\eta_p = \kappa_{e,p}/\kappa_p$ is the coupling efficiency for pump mode, α is the absorption coefficient as mentioned in the previous section, \tilde{r} is the frequency response of modal temperature modulation as a result of thermal diffusion, and the factor γ accounts for cross-phase modulation of the probe mode by the pump mode. The denominator in Eq. (7) creates a corner frequency for the response that is illustrated in the inset of Fig. 3a and that appears in the data and fitting in Fig. 3c.

The frequency response of the transmitted probe mode with respect to its resonance shift $\tilde{\delta}_b(\Omega)$ is derived in Supplementary Note II and has the following form:

$$\frac{\tilde{T}_b(\Omega)}{\tilde{\delta}_b(\Omega)} = -\frac{2\kappa_{e,b}\Delta_b^{(0)}}{\kappa_b^2/4 + (\Delta_b^{(0)})^2} \frac{\kappa_b - \kappa_{e,b} + i\Omega}{(\kappa_b/2 + i\Omega)^2 + (\Delta_b^{(0)})^2} |a_{\text{in},b}|^2, \quad (8)$$

where $\Delta_b^{(0)}$ is the steady-state detuning of the probe mode when no modulation is present, and κ_b and $\kappa_{e,b}$ refer to the total loss rate and external coupling rate for the probe mode.

The response curve in Fig. 3c is modeled by,

$$\tilde{\mathcal{R}}(\Omega) = \frac{\tilde{T}_b(\Omega)}{\tilde{P}_{in}(\Omega)} = \frac{\tilde{T}_b(\Omega) \tilde{\delta}_b(\Omega)}{\tilde{\delta}_b(\Omega) \tilde{P}_{in}(\Omega)} \quad (9)$$

and is fitted according to Eqs. (7) and (8). In the fitting, κ and κ_c have been measured separately, \tilde{r} is determined from finite element method simulations, and the probe mode Δ_0 and ratio a/g are parameters to be fitted.

Data availability

The data that support the plots within this paper and other findings of this study are available on figshare (<https://doi.org/10.6084/m9.figshare.c.5967105>). All other data used in this study are available from the corresponding author upon reasonable request.

Code availability

The analysis codes will be made available upon reasonable request.

Received: 30 November 2021; Accepted: 26 May 2022;

Published online: 09 June 2022

References

- Vahala, K. J. Optical microcavities. *Nature* **424**, 839 (2003).
- Spillane, S., Kippenberg, T. & Vahala, K. Ultralow-threshold Raman laser using a spherical dielectric microcavity. *Nature* **415**, 621–623 (2002).
- Kippenberg, T., Spillane, S. & Vahala, K. Kerr-nonlinear optical parametric oscillation in an ultrahigh-Q toroid microcavity. *Phys. Rev. Lett.* **93**, 083904 (2004).
- Lee, H. et al. Chemically etched ultrahigh-Q wedge-resonator on a silicon chip. *Nat. Photon.* **6**, 369–373 (2012).
- Schawlow, A. L. & Townes, C. H. Infrared and optical masers. *Phys. Rev.* **112**, 1940 (1958).
- Vahala, K. J. Back-action limit of linewidth in an optomechanical oscillator. *Phys. Rev. A* **78**, 023832 (2008).
- Li, J., Lee, H., Chen, T. & Vahala, K. J. Characterization of a high coherence Brillouin microcavity laser on silicon. *Opt. Express* **20**, 20170–20180 (2012).
- Aoki, T. et al. Observation of strong coupling between one atom and a monolithic microresonator. *Nature* **443**, 671–674 (2006).
- Lu, X. et al. Chip-integrated visible-telecom entangled photon pair source for quantum communication. *Nat. Phys.* **15**, 373–381 (2019).
- Lu, X. et al. Efficient telecom-to-visible spectral translation through ultralow power nonlinear nanophotonics. *Nat. Photon.* **13**, 593–601 (2019).
- Lukin, D. M. et al. 4H-silicon-carbide-on-insulator for integrated quantum and nonlinear photonics. *Nat. Photon.* **14**, 330–334 (2020).
- Ma, Z. et al. Ultrabright quantum photon sources on chip. *Phys. Rev. Lett.* **125**, 263602 (2020).
- Kippenberg, T. J. & Vahala, K. J. Cavity optomechanics: Back-action at the mesoscale. *Science* **321**, 1172–1176 (2008).
- Vollmer, F. & Yang, L. Label-free detection with high-Q microcavities: A review of biosensing mechanisms for integrated devices. *Nanophotonics* **1**, 267–291 (2012).
- Li, J., Lee, H. & Vahala, K. J. Microwave synthesizer using an on-chip Brillouin oscillator. *Nat. Commun.* **4**, 1–7 (2013).
- Kippenberg, T. J., Gaeta, A. L., Lipson, M. & Gorodetsky, M. L. Dissipative Kerr solitons in optical microresonators. *Science* **361**, eaan8083 (2018).
- Gundavarapu, S. et al. Sub-hertz fundamental linewidth photonic integrated Brillouin laser. *Nat. Photon.* **13**, 60–67 (2019).
- Jin, W. et al. Hertz-line-width semiconductor lasers using CMOS-ready ultrahigh-Q microresonators. *Nat. Photon.* **14**, 346–352 (2021).
- Li, J., Suh, M. G. & Vahala, K. J. Microresonator Brillouin gyroscope. *Optica* **4**, 346–348 (2017).
- Liang, W. et al. Resonant microphotonic gyroscope. *Optica* **4**, 114–117 (2017).
- Lai, Y.-H. et al. Earth rotation measured by a chip-scale ring laser gyroscope. *Nat. Photon.* **14**, 345–349 (2020).
- Ji, X. et al. Ultra-low-loss on-chip resonators with sub-milliwatt parametric oscillation threshold. *Optica* **4**, 619–624 (2017).
- Zhang, M., Wang, C., Cheng, R., Shams-Ansari, A. & Lončar, M. Monolithic ultra-high-Q lithium niobate microring resonator. *Optica* **4**, 1536–1537 (2017).
- Yang, K. Y. et al. Bridging ultrahigh-Q devices and photonic circuits. *Nat. Photon.* **12**, 297 (2018).
- Wilson, D. J. et al. Integrated gallium phosphide nonlinear photonics. *Nat. Photon.* **14**, 57–62 (2020).
- Chang, L. et al. Ultra-efficient frequency comb generation in AlGaAs-on-insulator microresonators. *Nat. Commun.* **11**, 1–8 (2020).
- Xie, W. et al. Ultrahigh-Q AlGaAs-on-insulator microresonators for integrated nonlinear photonics. *Opt. Express* **28**, 32894–32906 (2020).
- Liu, J. et al. Photonic microwave generation in the X- and K-band using integrated soliton microcombs. *Nat. Photon.* **14**, 486–491 (2020).
- Liu, X. et al. Aluminum nitride nanophotonics for beyond-octave soliton microcomb generation and self-referencing. *Nat. Commun.* **12**, 5428 (2021).
- Gao, R. et al. Broadband highly efficient nonlinear optical processes in on-chip integrated lithium niobate microdisk resonators of Q-factor above 10^8 . *New J. Phys.* **23**, 123027 (2021).
- Biberman, A., Shaw, M. J., Timurdogan, E., Wright, J. B. & Watts, M. R. Ultralow-loss silicon ring resonators. *Opt. Lett.* **37**, 4236–4238 (2012).
- Vernooy, D. W., Ilchenko, V. S., Mabuchi, H., Streed, E. W. & Kimble, H. J. High-Q measurements of fused-silica microspheres in the near infrared. *Opt. Lett.* **23**, 247–249 (1998).
- Pfeiffer, M. H. et al. Ultra-smooth silicon nitride waveguides based on the damascene reflow process: Fabrication and loss origins. *Optica* **5**, 884–892 (2018).
- Pfeiffer, M. H., Liu, J., Geiselmann, M. & Kippenberg, T. J. Coupling ideality of integrated planar high-Q microresonators. *Phys. Rev. Appl.* **7**, 024026 (2017).
- Spencer, D. T., Bauters, J. F., Heck, M. J. & Bowers, J. E. Integrated waveguide coupled Si₃N₄ resonators in the ultrahigh-Q regime. *Optica* **1**, 153–157 (2014).
- Liu, J. et al. Monolithic piezoelectric control of soliton microcombs. *Nature* **583**, 385–390 (2020).
- Xiang, C. et al. Laser soliton microcombs heterogeneously integrated on silicon. *Science* **373**, 99–103 (2021).
- Gorodetsky, M. L., Savchenkov, A. A. & Ilchenko, V. S. Ultimate Q of optical microsphere resonators. *Opt. Lett.* **21**, 453–455 (1996).
- Rokhsari, H., Spillane, S. & Vahala, K. Loss characterization in microcavities using the thermal bistability effect. *Appl. Phys. Lett.* **85**, 3029–3031 (2004).
- Liu, J. et al. Ultralow-power chip-based soliton microcombs for photonic integration. *Optica* **5**, 1347–1353 (2018).
- Puckett, M. W. et al. 422 million intrinsic quality factor planar integrated all-waveguide resonator with sub-mhz linewidth. *Nat. Commun.* **12**, 1–8 (2021).
- Parrain, D. et al. Origin of optical losses in gallium arsenide disk whispering gallery resonators. *Opt. Express* **23**, 19656–19672 (2015).
- Guha, B. et al. Surface-enhanced gallium arsenide photonic resonator with quality factor of 6×10^6 . *Optica* **4**, 218–221 (2017).
- An, K., Sones, B. A., Fang-Yen, C., Dasari, R. R. & Feld, M. S. Optical bistability induced by mirror absorption: Measurement of absorption coefficients at the sub-ppm level. *Opt. Lett.* **22**, 1433–1435 (1997).
- Rokhsari, H. & Vahala, K. J. Observation of Kerr nonlinearity in microcavities at room temperature. *Opt. Lett.* **30**, 427–429 (2005).
- Wang, T. et al. Rapid and high precision measurement of opto-thermal relaxation with pump-probe method. *Sci. Bull.* **63**, 287–292 (2018).
- Liu, J. et al. High-yield, wafer-scale fabrication of ultralow-loss, dispersion-engineered silicon nitride photonic circuits. *Nat. Commun.* **12**, 2236 (2021).
- Wu, L. et al. Greater than one billion q factor for on-chip microresonators. *Opt. Lett.* **45**, 5129–5131 (2020).
- Jung, H. et al. Tantalum Kerr nonlinear integrated photonics. *Optica* **8**, 811–817 (2021).
- Li, J., Lee, H., Yang, K. Y. & Vahala, K. J. Sideband spectroscopy and dispersion measurement in microcavities. *Opt. Express* **20**, 26337–26344 (2012).
- Carmon, T., Yang, L. & Vahala, K. Dynamical thermal behavior and thermal self-stability of microcavities. *Opt. Express* **12**, 4742–4750 (2004).
- Agrawal, G. P. *Nonlinear Fiber Optics* (Academic Press, 2007).
- Ikeda, K., Saperstein, R. E., Alic, N. & Fainman, Y. Thermal and Kerr nonlinear properties of plasma-deposited silicon nitride/silicon dioxide waveguides. *Opt. Express* **16**, 12987–12994 (2008).
- Pu, M., Ottaviano, L., Semenova, E. & Yvind, K. Efficient frequency comb generation in algaas-on-insulator. *Optica* **3**, 823–826 (2016).
- Li, J., Lee, H., Chen, T. & Vahala, K. J. Low-pump-power, low-phase-noise, and microwave to millimeter-wave repetition rate operation in microcombs. *Phys. Rev. Lett.* **109**, 233901 (2012).
- Yi, X., Yang, Q.-F., Yang, K. Y., Suh, M.-G. & Vahala, K. Soliton frequency comb at microwave rates in a high-Q silica microresonator. *Optica* **2**, 1078–1085 (2015).
- Miya, T., Terunuma, Y., Hosaka, T. & Miyashita, T. Ultimate low-loss single-mode fibre at 1.55 μm . *Electron. Lett.* **15**, 106–108 (1979).
- Pinard, L. et al. Toward a new generation of low-loss mirrors for the advanced gravitational waves interferometers. *Opt. Lett.* **36**, 1407–1409 (2011).
- Miller, R. C. Optical second harmonic generation in piezoelectric crystals. *Appl. Phys. Lett.* **5**, 17–19 (1964).
- Ettoumi, W., Petit, Y., Kasparian, J. & Wolf, J.-P. Generalized miller formulae. *Opt. Express* **18**, 6613–6620 (2010).

Acknowledgements

The authors thank H. Blauvelt and Z. Yuan for helpful comments, Z. Liu for discussions on data processing, as well as D. Carlson for preparing the Ta₂O₅ SEM image. Q.-X.J. acknowledges the Caltech Student Faculty Program for financial support. This work was supported by DARPA under the DODOS (HR0011-15-C-0055) and the APHi (FA9453-19-C-0029) programs.

Author contributions

M.G., Q.-F.Y., Q.-X.J., and J.L. conceived the idea. M.G., Q.-F.Y., and Q.-X.J. performed the measurement with assistance from H.W., L.W., and B.S. M.G., Q.-F.Y., Q.-X.J., and H.W. devised the theoretical model. L.W. fabricated the SiO₂ samples. J.L. and G.H. fabricated the Si₃N₄ samples. L.C. and W.X. fabricated the Al_{0.2}Ga_{0.8}As samples. S.-P.Y. fabricated the Ta₂O₅ samples. All the authors analyzed the data and wrote the manuscript. K.J.V., T.J.K., J.E.B., and S.B.P. supervised the project.

Competing interests

The authors declare no competing interests.

Additional information

Supplementary information The online version contains supplementary material available at <https://doi.org/10.1038/s41467-022-30966-5>.

Correspondence and requests for materials should be addressed to Scott B. Papp, John E. Bowers, Tobias J. Kippenberg or Kerry J. Vahala.

Peer review information *Nature Communications* thanks Vladimir Aksyuk and the other anonymous reviewer(s) for their contribution to the peer review of this work.

Reprints and permission information is available at <http://www.nature.com/reprints>

Publisher's note Springer Nature remains neutral with regard to jurisdictional claims in published maps and institutional affiliations.



Open Access This article is licensed under a Creative Commons Attribution 4.0 International License, which permits use, sharing, adaptation, distribution and reproduction in any medium or format, as long as you give appropriate credit to the original author(s) and the source, provide a link to the Creative Commons license, and indicate if changes were made. The images or other third party material in this article are included in the article's Creative Commons license, unless indicated otherwise in a credit line to the material. If material is not included in the article's Creative Commons license and your intended use is not permitted by statutory regulation or exceeds the permitted use, you will need to obtain permission directly from the copyright holder. To view a copy of this license, visit <http://creativecommons.org/licenses/by/4.0/>.

© The Author(s) 2022